Comparative study of structural and electrical properties of Pr and Ce doped BiFeO₃ ceramics synthesized by auto-combustion method

B. Stojadinović [a], Z. Dohčević-Mitrović [a, *], N. Paunović [a], N. Ilić [b], N. Tasić [b],
I. Petronijević [c], D. Popović [c], B. Stojanović [a]

[a] Center for Solid State Physics and New Materials, Institute of Physics Belgrade, University of Belgrade, Pregrevica 118, 11080 Belgrade, Serbia
[b] Institute for Multidisciplinary Research, University of Belgrade, Kneza Višeslava 1, 11000 Belgrade, Serbia
[c] Faculty of Physics, University of Belgrade, Studentski trg 12-16, 11000 Belgrade, Serbia

ABSTRACT

Polycrystalline $Bi_{1-x}Pr(Ce)_xFeO_3$ ceramics ($x = 0$, 0.03, 0.05 and 0.10) were prepared by auto-combustion method using urea as a fuel. The influence of Pr(Ce) doping on structural, vibrational, morphological, dielectric and ferroelectric properties of BiFeO₃ polycrystalline ceramics was investigated. From X-ray diffraction (XRD) and scanning electron microscopy measurements it was observed that Pr(Ce) doping generated a reduction of the crystallite (grain) size of BiFeO₃ and contraction of the rhombohedral cell due to the increased compressive strain. The changes seen in the XRD and Raman spectra of 10% Pr(Ce)-doped samples, pointed to a probable appearance of orthorhombic (pseudotetragonal) crystal structure. The pristine BiFeO₃ exhibited rounded shape, non-saturated ferroelectric hysteresis loop. The dielectric constant and dielectric loss have shown strong dispersion at lower frequencies, typical for conductive BiFeO₃. Dielectric and ferroelectric properties at room temperature were improved with Pr doping. Concerning the Ce-doped samples, only the 3% Ce-doped sample exhibited a better shaped hysteresis loop and improved dielectric properties compared to the pristine BiFeO₃. With further increase of Ce content the ferroelectric properties degraded.

© 2015 Elsevier B.V. All rights reserved.

1. Introduction

Materials which exhibit multiferroic behavior are very rare, and usually have low magnetic ordering temperature which constrains their application [1]. Among multiferroic materials, BiFeO₃ with a rhombohedrally distorted perovskite structure of space group R3c, belongs to a very few known magnetoelectric materials which exhibits both ferroelectricity and magnetic ordering at and above room temperature (ferroelectric Curie temperature $T_C \sim 1100$ K and Neel temperature $T_N \sim 640$ K) [2,3]. These features make BiFeO₃ particularly applicable in the fields of microelectronics, digital recording or magnetoelectric sensors [4,5]. BiFeO₃ can be potentially used in ferroelectric random access memory (FeRAM) applications [6] due to large spontaneous polarization [7–9], but of particular interest is to investigate the possible existence of magnetoelectric coupling in BiFeO₃ and its potential application in magnetic random access memories (MRAM) [10]. However, main disadvantages for the application of BiFeO₃ in devices is low resistivity (i.e. high leakage current) which causes large dielectric loss, poor ferroelectric loop at room temperature and small remnant polarization due to the presence of oxygen vacancies and secondary phases.

Doping of BiFeO₃ with rare earth ions at A-site [11–15], as well as doping with alkaline earth divalent ions such as Ca^{2+}, Ba^{2+} and Sr^{2+} [16] proved to be an effective way to improve its ferroelectric properties. In fact, A-site doping with ions of smaller radius influences the Fe–O–Fe bond angle, giving a more insulating character to BiFeO₃ [17]. The codoping with 4f elements at A-site and 3d elements at B-site is another effective way to reduce the leakage current in BiFeO₃ and to improve its multiferroic properties [18–21]. In the majority of previous reports referring the rare earth ions doping of BiFeO₃, only a few studies have been devoted to the investigation of ferroelectric properties of Pr(Ce)-doped BiFeO₃ ceramics [22–26] or thin films [27–29]. It can be expected that Bi substitution with $Pr^{3+/4+}(Ce^{3+/4+})$ ions will prevent Bi volatilization and reduce the oxygen vacancy concentration, enhancing at the

* Corresponding author.
E-mail address: zordoh@ipb.ac.rs (Z. Dohčević-Mitrović).

same time the insulating properties of $BiFeO_3$. Furthermore, Pr(Ce) doping can induce larger structural distortion and, even a structural transformation in $BiFeO_3$, which can have strong influence on ferroelectric properties of these materials [29,30].

In this paper, Pr(Ce)-doped $BiFeO_3$ ceramics were synthesized by auto-combustion method which represents a very facile, fast and low-cost method. A systematic study of the effect of Pr(Ce) doping on the structural, vibrational, ferroelectric, and dielectric properties of $BiFeO_3$ ceramics has been reported.

2. Experimental details

Pristine and Pr(Ce)-doped $BiFeO_3$ ($Bi_{1-x}Pr(Ce)_xFeO_3$, $x = 0.03$, 0.05 and 0.1) polycrystalline samples were synthesized by auto-combustion method using urea as a fuel. The fuel, besides providing the energy for the reaction, acts as a complexant and prevents the precipitation of metal ions in the form of hydroxides [31]. The $Bi_{1-x}Pr(Ce)_xFeO_3$ precursor solutions were prepared using $Bi(NO_3)_3 \cdot 6H_2O$ (Alfa Aesar, 98.0%), $Ce(NO_3)_3 \cdot 6H_2O$ (Acros Organics, 99.5%), $Pr(NO_3)_3 \cdot 6H_2O$ (Sigma–Aldrich, 99.9%), $Fe(NO_3)_3 \cdot 9H_2O$ (Alfa Aesar, 98.0–101.0%), HNO_3 (65%) and urea (Riedel-de Haen, 99.0–100.5%) as starting materials. The iron(III), cerium and praseodymium nitrates were dissolved in a minimal amount of distilled water, whereas bismuth nitrate was dissolved in a minimal amount of diluted nitric acid. The solutions were mixed and stirred for 15 min, after which the solution of urea was added. The molar ratio of urea to nitrates was 5:1. The obtained suspension was stirred and heated at 80–90 °C. During the heating a small amount of the precipitate, formed after urea addition, was dissolved and the clear solution was obtained. After a partial water evaporation, a yellow-white precipitate was formed and the solution was turned into gel. At the same time the self-ignition started. The reaction was fast and had finished in a few minutes. Large amount of gasses was released, without a flame. A black resin, remained after the auto-combustion reaction, was dried at 150–200 °C for one hour. The dried product was then grinded in a mortar and the obtained reddish powder was annealed at 600 °C for two hours with a heating rate of 10 °C/min. The powders were pressed into disks under the pressure of 300 MPa and sintered at 800 °C for 1 h in a closed dish, together with a small amount of Bi_2O_3 added in order to compensate the Bi loss during the heat treatment.

The structure and crystallinity of the $Bi_{1-x}Pr(Ce)_xFeO_3$ polycrystalline ceramics were investigated by X-ray diffraction (XRD) method, using Phillips PW1710 diffractometer with Cu Kα radiation. The surface morphology was studied by scanning electron microscopy (SEM, TESCAN SM-300). SEM micrographs were recorded on gold sputtered non-treated surfaces of ceramic samples.

Raman spectra were recorded in backscattering configuration using Tri Vista 557 Raman system equipped with a nitrogen-cooled CCD detector. The $\lambda = 514.5$ nm line of Ar^+/Kr^+ mixed laser was used as an excitation source with an incident laser power less than 60 mW in order to minimize the heating effects. The ferroelectric hysteresis loops were acquired at 1 kHz using a Radiant Precision Multiferroic Analyzer. The dielectric properties of the samples were examined in the frequency range from 80 Hz to 120 kHz using a Digital Programmable LCR Bridge HM8118 (Hameg). Each sample was placed in a closed capacitor cell housed in a Faraday cage with an AC signal of 1.5 V applied across the cell. The disk-shaped samples had a diameter close to the diameter of cell electrodes (8 mm). The same capacitor cell and Digital LCR Meter 4285A (HP/Agilent) were also used for the measurement of the dielectric properties at frequencies from 80 kHz to 8 MHz. All measurements were performed at room temperature.

3. Results and discussion

3.1. Structural and morphological properties

Fig. 1a shows XRD patterns of pristine $BiFeO_3$ and $Bi_{1-x}Pr_xFeO_3$ ceramics. All diffraction peaks of the pristine $BiFeO_3$ sample match with the rhombohedral structure (R3c) without the presence of a secondary phase. Polycrystalline $Bi_{1-x}Pr_xFeO_3$ samples crystallize in a slightly distorted R3c structure. The slight lattice distortion is manifested by a gradual shift of XRD peaks to higher 2θ values with Pr doping. The shift of XRD peaks to higher 2θ values can be ascribed to the unit cell contraction i.e. the decrease in lattice parameters due to the substitution of Bi^{3+} ions with smaller Pr dopant. The unit cell parameters of pristine $BiFeO_3$ and
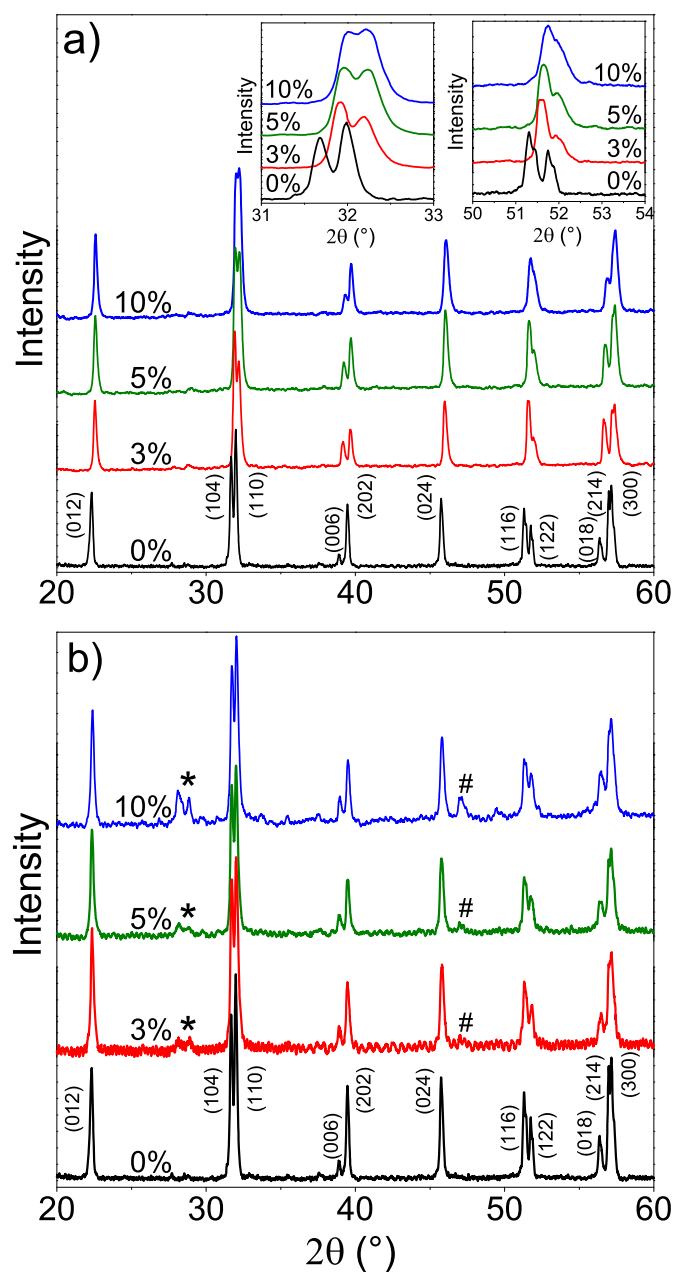

Fig. 1. X-ray diffraction patterns of the a) $Bi_{1-x}Pr_xFeO_3$ and b) $Bi_{1-x}Ce_xFeO_3$ samples ($0 \leq x \leq 0.1$). The (*) and (#) designate the appearance of additional phases discussed in the text.

$Bi_{1-x}Pr_xFeO_3$ samples are listed in Table 1. As can be seen from Table 1, with increasing Pr content, a reduction of both a and c lattice parameters, i.e. a contraction of the $BiFeO_3$ lattice, was observed.

The doublet peaks corresponding to the (104) and (110) planes around $2\theta \sim 32°$, and (116) and (122) planes around $2\theta \sim 52°$, with doping were shifted to higher 2θ values and almost merged into a single peak for the 10% Pr-doped sample. According to the literature data [32–34], these changes point to the beginning of partial phase transition from a rhombohedral (R3c) to an orthorhombic (Pbnm) structure. The enlarged 2θ regions where these peaks appear are presented in the insets of Fig. 1a. The partial structural transition can produce a distortion of the FeO_6 octahedron due to the changes in Fe–O bond length and O–Fe–O bond angles, affecting the electrical properties of $BiFeO_3$ [33,35]. Moreover, no additional peaks related to a secondary phase or other impurity phases have been observed in the sintered samples, implying a good solubility of Pr dopant in the $BiFeO_3$ lattice.

The XRD patterns of $Bi_{1-x}Ce_xFeO_3$ samples are presented in Fig. 1b and indexed to the rhombohedral $BiFeO_3$ structure. However, some weak diffraction peaks (marked with an asterisk) which correspond to a mullite ($Bi_2Fe_4O_9$) phase [36] appeared and became more pronounced with increased content of Ce dopant. As in the case of $Bi_{1-x}Pr_xFeO_3$ samples, lattice parameters (a and c) slightly decreased (see Table 1) implying that Ce substitution leads to the contraction of the unit cell and distortion of R3c structure. In addition, with increasing Ce content the peak at $2\theta \sim 46°$ (marked with #) splits into two peaks. This is particularly noticeable for the 10% Ce-doped sample. According to Liu et al. [29], these peaks can be indexed as (200) and (002) peaks of pseudotetragonal structure. Such a behavior suggests that in 10% Ce-doped sample partial structural transformation from a rhombohedral to the pseudotetragonal phase started.

The crystallite size and strain in the $Bi_{1-x}Pr(Ce)_xFeO_3$ polycrystalline samples were calculated using the Williamson-Hall (W–H) plots [37] and are presented in Table 1. The example of W–H plots for pure and 3% Pr(Ce)-doped $BiFeO_3$ samples are given in Fig. S1. From Table 1, it can be seen that the average crystallite size was reduced with doping, whereas the strain values increased and reached the highest value for the 10% Pr(Ce)-doped samples. It can be concluded that Pr(Ce) doping induces increased compressive strain responsible for the $BiFeO_3$ lattice contraction. The similar contraction of the $BiFeO_3$ lattice due to the compressive strain (stress) has been seen in Sm-doped $BiFeO_3$ thin films [38]. Furthermore, the increased strain in $Bi_{1-x}Pr(Ce)_xFeO_3$ samples can produce a distortion of rhomohedral structure, which can induce gradual structural phase transformation as in a case of Y-doped $BiFeO_3$ nanopowders [39].

The surface morphology of $BiFeO_3$ and $Bi_{1-x}Pr(Ce)_xFeO_3$ ($x = 0.05, 0.1$) samples is shown in Fig. 2. The undoped (Fig. 2a) and Pr-doped $BiFeO_3$ samples (Fig. 2b and c) exhibit rather dense microstructure (82 and 78% of the theoretical density for undoped $BiFeO_3$ and 10% Pr-doped samples) with a clearly visible grains and
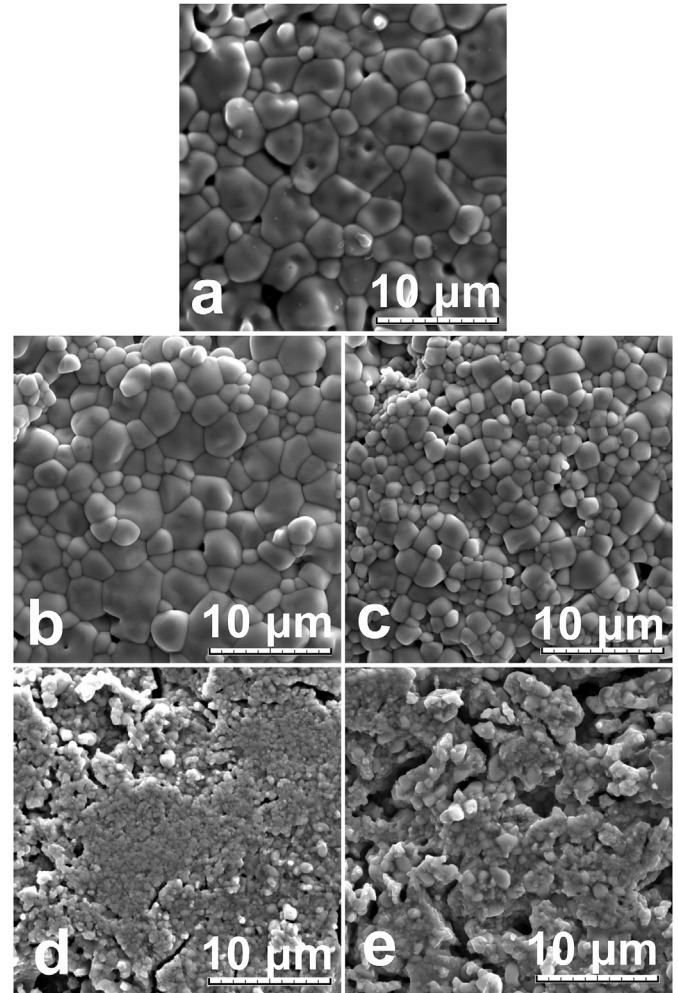

Fig. 2. SEM images of the surface morphology of a) $BiFeO_3$, b) $Bi_{0.95}Pr_{0.05}FeO_3$, c) $Bi_{0.90}Pr_{0.10}FeO_3$, d) $Bi_{0.95}Ce_{0.05}FeO_3$, and e) $Bi_{0.90}Ce_{0.10}FeO_3$ samples.

grain boundary. The morphology of Ce-doped samples (Fig. 2d and e) is different from that of pure and Pr-doped samples. These samples exhibit less pronounced grain boundary microstructure with increased intergranular porosity and lower sample density (65% of the theoretical density for 10% Ce-doped sample). SEM images showed that in Pr(Ce)-doped samples the grain size decreased. The grain size decrease in Pr(Ce)-doped samples can be explained by inhibiting effect of increased Pr(Ce) dopant content on grain growth or can be attributed to the suppressed oxygen vacancy formation in these samples, as oxygen vacancies favorize the grain growth during the sintering process [33]. In addition, if there is a decrease of oxygen vacancy concentration, the reaction rate in the solid phase is slowed down, grains remain smaller and the

Table 1
The lattice parameters, average crystallite size and strain values for $Bi_{1-x}Pr(Ce)_xFeO_3$ samples.

Samples	Lattice parameter a (Å)	Lattice parameter c (Å)	Strain (%)	Crystalite size (nm)
$BiFeO_3$	5.617 ± 0.004	13.760 ± 0.010	0.10 ± 0.02	28.9 ± 2.2
$Bi_{0.97}Pr_{0.03}FeO_3$	5.587 ± 0.005	13.686 ± 0.012	0.16 ± 0.03	22.2 ± 1.6
$Bi_{0.95}Pr_{0.05}FeO_3$	5.582 ± 0.003	13.672 ± 0.007	0.18 ± 0.04	21.9 ± 1.9
$Bi_{0.90}Pr_{0.10}FeO_3$	5.576 ± 0.004	13.657 ± 0.009	0.36 ± 0.05	19.3 ± 1.9
$Bi_{0.97}Ce_{0.03}FeO_3$	5.597 ± 0.004	13.735 ± 0.013	0.20 ± 0.01	25.2 ± 0.9
$Bi_{0.95}Ce_{0.05}FeO_3$	5.598 ± 0.005	13.736 ± 0.010	0.24 ± 0.01	24.0 ± 1.6
$Bi_{0.90}Ce_{0.10}FeO_3$	5.595 ± 0.003	13.730 ± 0.011	0.32 ± 0.04	22.9 ± 2.6

densification is weaker.

3.2. Raman analysis

The structural evolution of $BiFeO_3$ structure with Pr(Ce) ion substitution can be reflected through the Raman spectra as well. For R3c rhombohedral structure, the group theory analysis predicts 13 Raman active modes (4 A_1 and 9 doubly degenerate E modes) [40–45], but the number of clearly seen Raman modes at room temperature is much less than predicted [43]. The room

temperature Raman spectra of $BiFeO_3$ and $Bi_{1-x}Pr(Ce)_xFeO_3$ samples are presented in Fig. 3.

In the Raman spectrum of $BiFeO_3$ sample (Fig. 3a), two A_1 modes at 171 and around 218 cm^{-1} [39] and two E modes at 75 and 265 cm^{-1} [43] can be clearly seen. The strong and wide Raman peak at 136 cm^{-1} is composed of two modes, E mode at 132 cm^{-1} and A_1 mode at around 140 cm^{-1}, which can be resolved by parallel polarization measurements at low temperatures [43]. The other E phonon modes at around 330, 368, 428, 475, 520 and 599 cm^{-1} are barely visible. In the Raman spectra of $Bi_{1-x}Pr_xFeO_3$ samples, the E mode at 75 cm^{-1} and A_1 mode at around 218 cm^{-1} exhibit shift to higher frequencies. The Raman peak at 136 cm^{-1} is also shifted to higher frequencies. After deconvolution of the 136 cm^{-1} peak using Lorentzian profiles, the position of the E mode remained unchanged, whereas the A_1 mode was shifted to higher frequencies (see dashed line in Fig. 3a). The other E modes (around 475, 520 and 599 cm^{-1}) become more prominent with increasing Pr content. In the Raman spectra of $Bi_{1-x}Ce_xFeO_3$ samples, more pronounced changes in the Raman modes position and intensity are observed in the case of 10% Ce-doped sample.

The exact positions of the Raman modes in the 10% Pr(Ce)-doped samples, for which the possible structural phase transformation was observed, were determined using the Lorentzian fit. In Fig. 3c are shown the deconvoluted Raman spectra of $BiFeO_3$, $Bi_{0.90}Pr_{0.10}FeO_3$ and $Bi_{0.90}Ce_{0.10}FeO_3$ samples. The obtained mode positions are summarized in Table 2.

As can be seen from Table 2, the E and A_1 modes (75, 140 cm^{-1}) which are related to Bi−O bonds, as well as the E modes (428, 520 and 599 cm^{-1}) which are characteristic for the Fe−O bonds [44,46], are shifted to higher frequencies for both $Bi_{0.90}Pr_{0.10}FeO_3$ and $Bi_{0.90}Ce_{0.10}FeO_3$ samples. The A_1 mode at around 218 cm^{-1}, which is characteristic for Bi−O bonds is shifted to higher frequencies in $Bi_{0.90}Pr_{0.10}FeO_3$ sample. The blueshift of the E and A_1 modes, for which the contribution of Bi−O bonds dominates, is expected when the substitution with smaller atomic mass Pr(Ce) ions at Bi-site happens, because the Raman mode frequency is dependent on the atomic mass (M) of the substituent according to the relation $\omega \sim (k/M)^{1/2}$ [22,26]. The appearance of the increased compressive strain in $BiFeO_3$ lattice with increased amount of Pr(Ce) dopant is also responsible for the blueshift of the frequency of the Raman A_1 and E modes, characteristic for both Bi−O and Fe−O bonds.

The E mode at 599 cm^{-1}, which is of low intensity in the pristine $BiFeO_3$ and almost invisible in $Bi_{0.90}Ce_{0.10}FeO_3$, becomes very prominent in $Bi_{0.90}Pr_{0.10}FeO_3$ sample. Compared to the pristine $BiFeO_3$, the relative intensity ratio of A_1 modes at about 140 and 171 cm^{-1} (I_{140}/I_{171}) is increased in 10% Pr(Ce)-doped samples ($I_{140}/I_{171} = 0.69$, 1.1, and 2.1 for $BiFeO_3$, 10% Ce and 10% Pr-doped samples, respectively). The change of the relative intensity of these two A_1
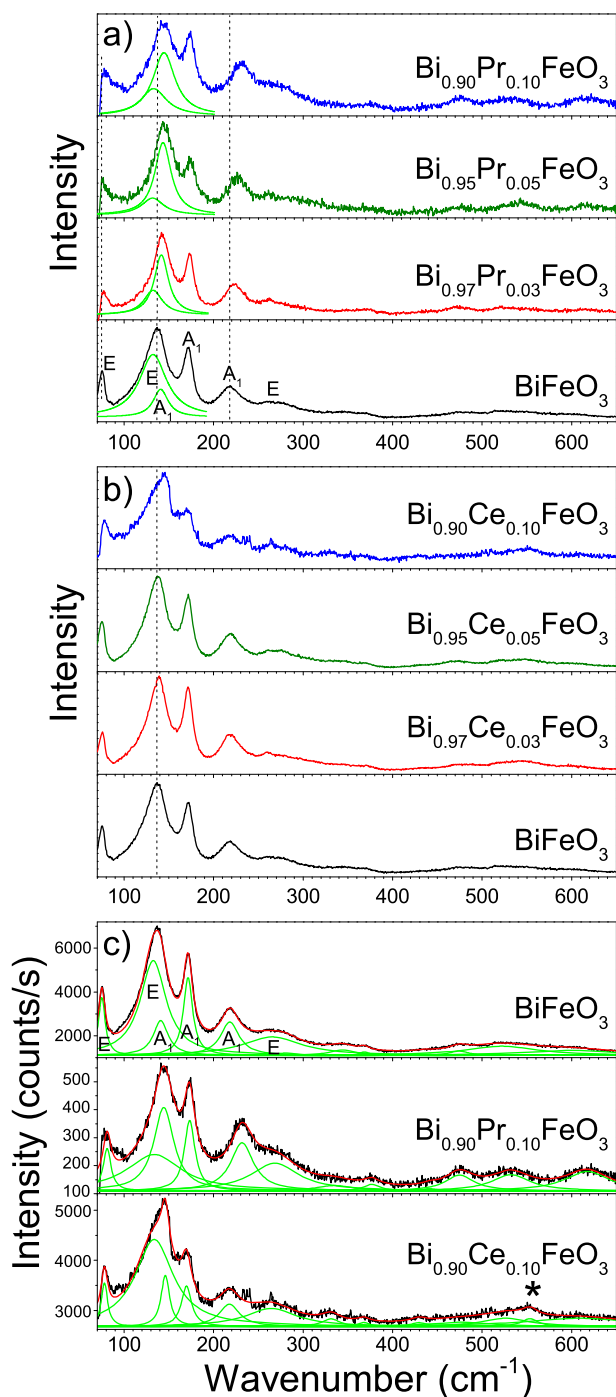
Fig. 3. Room-temperature Raman spectra of (a) $Bi_{1-x}Pr_xFeO_3$ and (b) $Bi_{1-x}Ce_xFeO_3$ samples ($0 \leq x \leq 0.1$), together with (c) deconvoluted Raman spectra of $BiFeO_3$, $Bi_{0.90}Pr_{0.10}FeO_3$ and $Bi_{0.90}Ce_{0.10}FeO_3$ samples.

Table 2
Positions of the Raman modes for $BiFeO_3$, $Bi_{0.90}Pr_{0.10}FeO_3$, and $Bi_{0.90}Ce_{0.10}FeO_3$ samples.

Raman modes (in cm^{-1})	$BiFeO_3$	$Bi_{0.90}Pr_{0.10}FeO_3$	$Bi_{0.90}Ce_{0.10}FeO_3$
E	75.4	81.2	77.4
E	132.3	132.9	132.7
A_1	140.8	144.5	145.0
A_1	171.2	172.7	169.6
A_1	218.7	231.6	217.5
E	265.2	269.0	265.1
E	330.6	333.3	331.3
E	368.6	376.0	367.1
E	428.4	440.6	429.2
E	475.8	475.0	476.8
E	520.4	532.8	526.9
E	599.2	617.7	611.7

modes reflects the change in Bi–O bonds and the stereochemical activity of Bi lone electron pair with Pr(Ce) doping [23]. Furthermore, any changes in the position or intensity of the 140, 171 and 599 cm^{-1} modes are related to the changes in the ferroelectric properties of $BiFeO_3$ as well [22,45]. In the Raman spectrum of $Bi_{0.90}Ce_{0.10}FeO_3$ appears an additional mode (marked with an asterisk in Fig. 3c) at around 553 cm^{-1}. This mode can be ascribed to the mode of $Bi_2Fe_4O_9$ phase [47]. The appearance of this mode is in accordance with the XRD pattern of $Bi_{0.90}Ce_{0.10}FeO_3$ in which the presence of a mullite phase has been seen. The changes observed in the Raman spectra of doped samples gave a clear evidence about the lattice distortion induced by Pr(Ce) doping.

3.3. Dielectric properties

The frequency dependence of the dielectric constant (ε') and loss tangent (tan δ) of $Bi_{1-x}Pr(Ce)_xFeO_3$ samples are shown in Fig. 4. It can be observed from Fig. 4a that the dielectric constant of the pristine $BiFeO_3$ at low frequencies has the highest value ($\varepsilon' = 159$) and shows a strong dispersion in the low-frequency region. Such a behavior is characteristic for the presence of oxygen or bismuth vacancies, which are responsible for the appearance of charge carriers at grain boundaries or interfaces (i.e. the local space charge), and an increased conductivity in $BiFeO_3$ [48]. The contribution of the local space charge to the dielectric constant usually manifests as a strong dispersion at low frequencies. The presence of oxygen vacancies also increases the probability of a hopping conduction mechanism between Fe^{2+} and Fe^{3+} ions, which can be reflected through an increased value of the dielectric constant [48].

The dielectric constant of Pr(Ce)-doped samples significantly decreases and exhibits much smaller dispersion at low frequencies (Fig. 4a). The overall decrease of the dielectric constant can be attributed to a reduced conductivity and a decreased space charge relaxation at the interface [49], but can also originate from the contraction of the unit cell volume when Bi ions are substituted with smaller Pr(Ce) ions. The unit cell contraction can result in a decreased polarization because of less free volume for the displacement of Fe^{3+} ions in FeO_6 octahedra. The dielectric constant of $Bi_{1-x}Pr_xFeO_3$ samples exhibits relatively small ($x = 0.03, 0.05$) or almost no dielectric dispersion ($x = 0.1$). Such a behavior can be explained by the fact that the incorporation of $Pr^{3+/4+}$ ions into the $BiFeO_3$ lattice reduces the oxygen vacancy concentration and conductivity of $BiFeO_3$ [49, 29]. Ce-doped samples ($x = 0.03, 0.05$) have lower value of dielectric constant

than Pr-doped ones and show almost no frequency dispersion. The value of dielectric constant and its dispersion increases for the $Bi_{0.90}Ce_{0.10}FeO_3$ sample. The increase of dielectric constant can originate from the increased oxygen vacancy concentration and the appearance of local space charges at the grain boundaries or interfaces [48,49]. The change of the dielectric constant with frequency in $BiFeO_3$ and $Bi_{1-x}Pr(Ce)_xFeO_3$ samples can be well explained by the Maxwell–Wagner relaxation effect which refers to the interfacial polarization [48,49].

The loss tangent (tan δ) shows a similar variation with frequency as the dielectric constant. At low frequencies, the loss tangent of the undoped $BiFeO_3$ sample shows a higher value, due to the increased defect concentration and conductivity and shows a broad relaxation peak in the intermediate frequency range (10 kHz–1 MHz). The broad relaxation peaks are usually caused by inhomogenous grain conductivity [49]. The tan δ curves show dispersive characteristics in the low-frequency region for Pr-doped samples, with much less pronounced relaxation peaks. At frequencies higher than 10 kHz, the value of tan δ is reduced and is significantly lower than in the pristine $BiFeO_3$, due to reduced oxygen vacancy concentration and conductivity. The Ce-doped samples with lower content of Ce ($x = 0.03, 0.05$) have low value of tan δ over the whole frequency range. The tan δ becomes much higher in the case of $Bi_{0.90}Ce_{0.10}FeO_3$ sample, pointing to increased conductivity of $Bi_{0.90}Ce_{0.10}FeO_3$ sample.

3.4. Ferroelectric properties

The ferroelectric hysteresis (P–E) loops for $Bi_{1-x}Pr(Ce)_xFeO_3$ samples are presented in Fig. 5. In the inset of Fig. 5b is given P–E loop of the pristine $BiFeO_3$.

The $BiFeO_3$ exhibited a rounded shape i.e. a non-saturated (lossy) P–E loop, and was not able to withstand applied electric field stronger than 2 kV, which is typical for a conductive $BiFeO_3$ material. The ferroelectric performances of pristine $BiFeO_3$ are consistent with the dielectric measurements. The ferroelectric loops of the Pr(Ce)-doped samples (Fig. 5a and b), exhibited less pronounced leakage effect than for the pristine $BiFeO_3$, but were still non-saturated. This is an expected behavior, since the incorporation of $Pr^{3+/4+}(Ce^{3+/4+})$ ions in the $BiFeO_3$ lattice should suppress the formation of bismuth and oxygen vacancies. With increasing Pr content, the maximal polarization (P_M) and the remnant polarization (P_R) have increased and reached the values of 0.4 and 0.35 μC/cm^2 for $Bi_{0.90}Pr_{0.10}FeO_3$. The P_M and P_R values are comparable with the previously reported data on $BiFeO_3$ ceramics

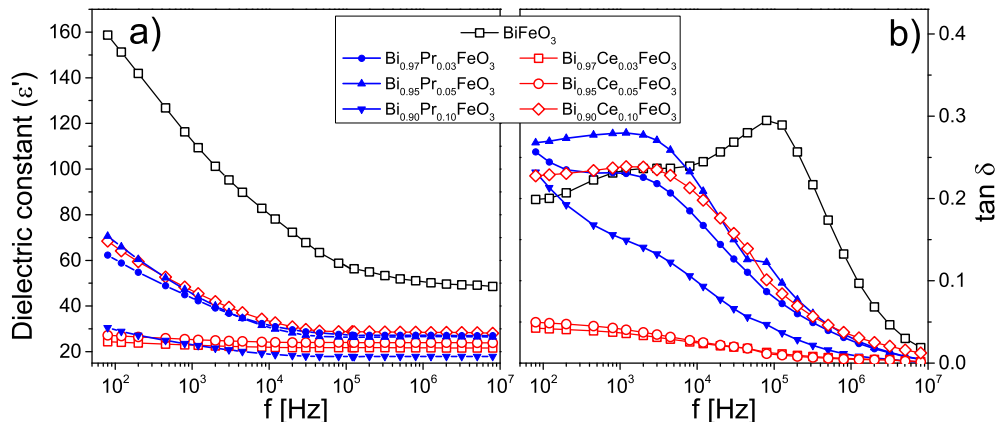**Fig. 4.** Room temperature (a) dielectric constant (ε') and (b) loss tangent (tan δ) of $Bi_{1-x}Pr(Ce)_xFeO_3$ samples ($0 \leq x \leq 0.1$) as a function of frequency.
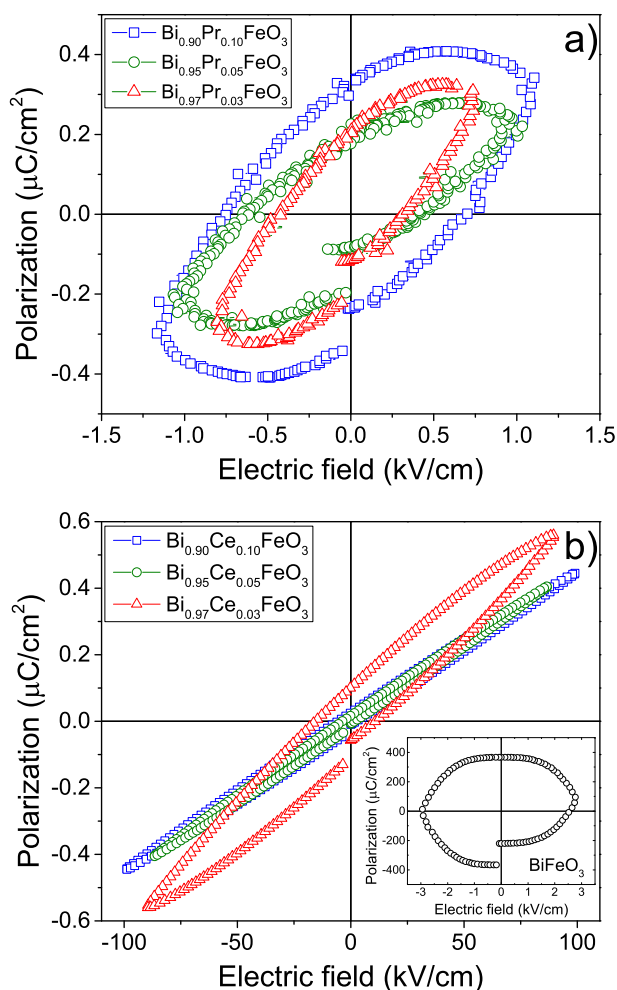
Fig. 5. Room-temperature P–E hysteresis loops for (a) $Bi_{1-x}Pr_xFeO_3$ and (b) $Bi_{1-x}Ce_xFeO_3$ samples ($0.03 \leq x \leq 0.1$). In the inset is presented P–E hysteresis loop for the pristine $BiFeO_3$.

distortion of R3c structure and in 10% Pr(Ce) doped samples, there is an indication that partial structural phase transformation from rhombohedral to orthorhombic (pseudotetragonal) phase started. Pr doping suppresses the formation of oxygen vacancies, decreasing the conductivity of Pr-doped $BiFeO_3$ samples. In the case of Ce-doped samples, improved dielectric and ferroelectric properties exhibited the sample with 3% of Ce. Further increase of Ce content caused the deterioration of ferroelectric properties and in the 10% Ce-doped sample both the dielectric and ferroelectric properties of $BiFeO_3$ ceramics were degraded. The reduction of ferroelectric polarization for $Bi_{0.95}Ce_{0.05}FeO_3$ sample can originate from the presence of impurity $Bi_2Fe_4O_9$ phase which increases the conductivity of $BiFeO_3$. Further, deterioration of dielectric and ferroelectric properties for $Bi_{0.90}Ce_{0.10}FeO_3$ can originate from lower percentage of Ce^{4+} ions in this sample (see Fig. S2 Supplementary material) and increasing content of $Bi_2Fe_4O_9$ phase. On the other hand, the increased Ce content can decrease the stereochemical activity of Bi ions and can lead to the partial transition from ferroelectric to paraelectric phase, like in La-doped $BiFeO_3$ [54].

4. Conclusion

In summary, polycrystalline $Bi_{1-x}Pr(Ce)_xFeO_3$ ceramics ($x = 0$, 0.03, 0.05 and 0.10) were prepared by auto-combustion method. SEM and XRD analysis have shown that the crystallite and grain sizes slightly decreased in Pr(Ce)-doped samples, whereas the compressive strain increased. XRD and Raman spectra of 10% Pr(Ce)-doped samples pointed to probable appearance of orthorhombic (pseudotetragonal) phase. The presence of secondary phase was evident only in Ce-doped samples. The pristine $BiFeO_3$ showed lossy P–E loop, large dispersion of dielectric constant and tan δ at low frequencies, and a broad relaxation peak in tan δ in the intermediate frequency range. The dielectric properties were improved by the Pr substitution, i.e. the dielectric constant had lower values than in the pristine $BiFeO_3$ and exhibited smaller or almost no dispersion in the investigated frequency range, whereas with increasing Pr content the loss tangent decreased and had low values at higher frequencies. Pr-doped samples exhibited better shaped ferroelectric loops with much less pronounced leakage effect. The remnant and maximal polarization increased with increased Pr doping. Such an improvement in dielectric and ferroelectric properties can be attributed to decreased interfacial polarization and reduced conductivity of $BiFeO_3$ ceramic samples. Regarding the Ce-doped samples, the best dielectric and ferroelectric properties were observed in the 3% Ce-doped sample, whereas with further increase of Ce dopant up to 10% these properties were degraded. The reduced polarization and increased dielectric loss may be attributed to the appearance of conducting $Bi_2Fe_4O_9$ phase and decreased stereochemical activity of Bi-sites by Ce doping due to the possible appearance of the pseudotetragonal phase.

Appendix A. Supplementary data

Supplementary data related to this article can be found at http://dx.doi.org/10.1016/j.jallcom.2015.09.235.

doped with similar content of Pr [24,49]. However, the breakdown electric field for Pr-doped samples is still as low as in the case of the pristine $BiFeO_3$.

Initial Ce doping increases the ability of $BiFeO_3$ to withstand higher electric fields [50], in our case up to 100 kV/cm. This enhancement can be attributed to a decrease of oxygen vacancy concentration, as the substitution of Bi ions with higher valence Ce^{4+} ions would suppress the formation of oxygen vacancies and consequently reduce the leakage current. The polarization has the highest value of about 0.56 μC/cm^2 in the 3% Ce-doped sample, and the P_R value is about 0.1 μC/cm^2. With further increase of Ce content, the values of P_M, P_R and coercive field decreased and the samples exhibited a poor P–E loop. This result suggests that the ferroelectric properties were degraded with further increase of Ce content.

Several reasons can be responsible for the lower values of P_R in Pr(Ce)-doped samples. The contraction of $BiFeO_3$ unit cell with Pr(Ce) doping, i.e. the partial phase transition from rhombohedral to orthorhombic (pseudotetragonal) phase can reduce the remnant polarization, as the direction of the spontaneous polarization can be changed [51,29]. Another reason can be found in lowering of the crystal anisotropy and a decrease of Curie temperature with rare earth ion doping [52,53].

Therefore, we can conclude that Pr(Ce) doping causes a

References

[1] N.A. Spaldin, Science 309 (2005) 391.
[2] I. Sosnowska, T. Peterlin-Neumaier, E. Steichele, J. Phys. C: Solid State Phys. 15 (1982) 4835–4846.
[3] G. Catalan, J.F. Scott, Adv. Mater. 21 (2009) 2463–2485.
[4] R. Ramesh, N.A. Spaldin, Nat. Mater. 6 (2007) 21–29.
[5] S.-W. Cheong, M. Mostovoy, Nat. Mater. 6 (2007) 13–20.
[6] A.N. Kalinkin, E.M. Kozhbakhteev, A.E. Polyakov, V.M. Skorikov, Inorg. Mater. 49 (2013) 1031–1043.
[7] C. Ederer, N.A. Spaldin, Phys. Rev. Lett. 95 (2005) 257601.
[8] J. Li, J. Wang, M. Wuttig, R. Ramesh, N. Wang, B. Ruette, A.P. Pyatakov, A.K. Zvezdin, D. Viehland, Appl. Phys. Lett. 84 (2004) 5261–5263.
[9] K.Y. Yun, D. Ricinschi, T. Kanashima, M. Noda, M. Okuyama, Jpn. J. Appl. Phys. 43 (2004) L647–L648.
[10] J.F. Scott, Nat. Mater. 6 (2007) 256–257.
[11] S.B. Emery, C.J. Cheng, D. Kan, F.J. Rueckert, S.P. Alpay, V. Nagarajan, I. Takeuchi, B.O. Wells, Appl. Phys. Lett. 97 (2010) 152902.
[12] K.S. Nalwa, A. Garg, A. Upadhyaya, Mater. Lett. 62 (2008) 878–881.
[13] G.L. Yuan, S.W. Or, J.M. Liu, Z.G. Liu, Appl. Phys. Lett. 89 (2006) 052905.
[14] J.H. Lee, H.J. Choi, D. Lee, M.G. Kim, C.W. Bark, S. Ryu, M.A. Oak, H.M. Jang, Phys. Rev. B 82 (2010) 045113.
[15] G.S. Lotey, N.K. Verma, J. Nanopart. Res. 14 (2012) 742.
[16] V.A. Khomchenko, D.A. Kiselev, J.M. Vieira, L. Jian, A.L. Kholkin, A.M.L. Lopes, Y.G. Pogorelov, J.P. Araujo, M. Maglione, J. Appl. Phys. 103 (2008) 024105.
[17] C.H. Yang, D. Kan, I. Takeuchi, V. Nagarajan, J. Seidel, Phys. Chem. Chem. Phys. 14 (2012) 15953–15962.
[18] W. Liu, G. Tan, X. Xue, G. Dong, H. Ren, A. Xia, Ceram. Int. 40 (2014) 12179–12185.
[19] W. Ye, G. Tan, G. Dong, H. Ren, A. Xia, Ceram. Int. 41 (2015) 4668–4674.
[20] Y.J. Kim, J.W. Kim, C.M. Raghavan, J.J. Oak, H.J. Kim, W.J. Kim, M.H. Kim, T.K. Song, S.S. Kim, Ceram. Int. 39 (2013) S195–S199.
[21] C.M. Raghavan, J.W. Kim, S.S. Kim, Ceram. Int. 39 (2013) 3563–3568.
[22] D. Varshney, P. Sharma, S. Satapathy, P.K. Gupta, J. Alloys Compd. 584 (2014) 232–239.
[23] P. Sharma, D. Varshney, S. Satapathy, P.K. Gupta, Mater. Chem. Phys. 143 (2014) 629–636.
[24] N. Kumar, N. Panwar, B. Gahtori, N. Singh, H. Kishan, V.P.S. Awana, J. Alloy. Compd. 501 (2010) L29–L32.
[25] S.K. Pradhan, B.K. Roul, Phys. B 407 (2012) 2527–2532.
[26] M. Arora, M. Kumar, Ceram. Int. 41 (2015) 5705–5712.
[27] B. Yu, M. Li, Z. Hu, L. Pei, D. Guo, X. Zhao, S. Dong, Appl. Phys. Lett. 93 (2008) 182909.
[28] X. Wang, H. Liu, B. Yan, J. Eur. Ceram. Soc. 29 (2009) 1183–1187.
[29] J. Liu, M. Li, L. Pei, J. Wang, B. Yu, X. Wang, X. Zhao, J. Alloy. Compd. 493 (2010) 544–548.
[30] J. Liu, M. Li, L. Pei, B. Yu, D. Guo, X. Zhao, J. Phys. D. Appl. Phys. 42 (2009) 115409.
[31] S. Lorentzou, K. Karadimitra, C. Agrafiotis, A.G. Konstandopoulos, in: Proceedings of the PARTEC 2004, International Conference for Particle Technology, Nuremberg, Germany, March 16–18, 2004.
[32] L. Chen, L. Zheng, Y. He, J. Zhang, Z. Mao, X. Chen, J. Alloys Compd. 633 (2015) 216–219.
[33] P.C. Sati, M. Arora, S. Chauhan, M. Kumar, S. Chhoker, Ceram. Int. 40 (2014) 7805–7816.
[34] V. Singh, S. Sharma, M. Kumar, R.K. Kotnala, R.K. Dwivedi, J. Magn. Magn. Mater. 349 (2014) 264–267.
[35] S.K. Pradhan, B.K. Roul, J. Phys. Chem. Solids 72 (2011) 1180–1187.
[36] N.I. Ilić, A.S. Džunuzović, J.D. Bobić, B.S. Stojadinović, P. Hammer, M.M. Vijatović Petrović, Z.D. Dohčević-Mitrović, B.D. Stojanović, Ceram. Int. 41 (2015) 69–77.
[37] G.K. Williamson, W. Hall, Acta Metall. 1 (1953) 22–31.
[38] X. Xu, T. Guoqiangn, R. Huijun, X. Ao, Ceram. Int. 39 (2013) 6223–6228.
[39] R.K. Mishra, D.K. Pradhan, R.N.P. Choudhary, A. Banerjee, J. Phys. Condens. Matter 20 (2008) 045218.
[40] M.N. Iliev, M.V. Abrashev, D. Mazumdar, V. Shelke, A. Gupta, Phys. Rev. B 82 (2010) 014107.
[41] M.K. Singh, H.M. Jang, S. Ryu, M.H. Jo, Appl. Phys. Lett. 88 (2006) 42907.
[42] P. Hermet, M. Goffinet, J. Kreisel, Ph. Ghosez, Phys. Rev. B 75 (2007) 220102(R).
[43] H. Fukumura, S. Matsui, H. Harima, T. Takahashi, T. Itoh, K. Kisoda, M. Tamada, Y. Noguchi, M. Miyayama, J. Phys. Condens. Matter 19 (2007) 365224.
[44] M.K. Singh, S. Ryu, H.M. Jang, Phys. Rev. B 72 (2005) 132101.
[45] G.L. Yuan, S.W. Or, H.L. Chan, Z.G. Liu, J. Appl. Phys. 101 (2007) 024106.
[46] Y. Yao, W. Liu, Yu Chan, C. Leung, C. Mak, B. Ploss, Int. J. Appl. Ceram. Technol. 8 (2011) 1246–1253.
[47] M.N. Iliev, A.P. Litvinchuk, V.G. Hadjiev, M.M. Gospodinov, V. Skumryev, E. Ressouche, Phys. Rev. B 81 (2010) 024302.
[48] A. Reetu, S. Agarwal, Ashima Sanghi, J. Appl. Phys. 110 (2011) 073909.
[49] V. Kumar, A. Gaur, N. Sharma, J. Shah, R.K. Kotnala, Ceram. Int. 39 (2013) 8113–8121.
[50] Z. Quan, W. Liu, H. Hu, S. Xu, B. Sebo, G. Fang, M. Li, X. Zhao, J. Appl. Phys. 104 (2008) 084106.
[51] X. Li, X. Wang, Y. Li, W. Mao, P. Li, T. Yang, J. Yang, Mater. Lett. 90 (2013) 152–155.
[52] H. Ushida, R. Ueno, H. Funakubo, S. Koda, J. Appl. Phys. 100 (2006) 014106.
[53] P. Pandit, S. Satapathy, P. Sharma, P.K. Gupta, S.M. Yusuf, V.G. Sathe, Bull. Mater. Sci. 34 (2011) 899–905.
[54] G.L. Yuan, S.W. Or, H.L. Chan, J. Phys. D. Appl. Phys. 40 (2007) 1196–1200.